Mix and measure - combining *in situ* X-ray powder diffraction and microtomography for accurate hydrating cement studies

S. Shirani,[1] A. Cuesta,[1] A.G. De la Torre,[1] I. Santacruz,[1] A. Morales-Cantero,[1] I. Koufany,[1] C. Redondo-Soto,[1] I.R. Salcedo,[2] L. León-Reina,[2] M.A.G. Aranda[1,*]

[1]Departamento de Química Inorgánica, Cristalografía y Mineralogía, Universidad de Málaga, Málaga, 29071, Spain

[2]Servicios Centrales de Apoyo a la Investigación, Universidad de Málaga, 29071 Málaga, Spain

* email: g_aranda@uma.es

Abstract:

It is reported an innovative methodology based on *in situ* $MoK\alpha_1$ laboratory X-ray powder diffraction (LXRPD) and microtomography (μCT) avoiding any sample conditioning. The pastes are injected in 2.0 mm capillaries and the extremes are just sealed. The measurements take place in the same region of the hydrating paste. Thick capillaries are key to avoiding self-desiccation, which dictates the need of high-energy X-ray radiation for the diffraction study. This approach has been tested with a PC 42.5 R paste having w/c=0.50. μCT data were collected at 12 hours and 1, 3, 7 and 79 days. LXRPD data were acquired at 1, 3, 7 and 77 days. In this proof-of-principle research, the same paste was also cured *ex situ*. Portlandite contents obtained by thermal analysis, *ex situ* powder diffraction, *in situ* mass balance calculation and *in situ* powder diffraction were 13.8, 13.1, 13.1 and 12.5 wt%, respectively. From the μCT study, the grey value histogram evolution with time showed a crossing point which allowed us to distinguish (appearing) hydrated products from (dissolving) unhydrated cement particles. Segmentations were carried out by global thresholding and the random forest approach (one type of supervised Machine Learning). The comparison of the segmented results for the unhydrated cement fraction and the Rietveld quantitative phase analysis outputs gave an agreement of 2%. The potential of this methodology to deal with more complex binders is also presented.

Keywords: Portland cement hydration; Rietveld analysis; microCT; 4D X-ray imaging

1. Introduction

Understanding of the hydration of Portland cements (PC), at the different length scales, is puzzling because of the interaction of many intervening parameters [1,2]. PC are multiphase materials with variable (i) elemental compositions, (ii) phase contents, (iii) textural properties (particle size distributions and specific surface areas of the different components), and an increasing trend of using inorganic additions and organic admixtures. Moreover, the hydration processes occur under variable conditions, including but not restricted to, (i) water-to-cement mass ratio (w/c), (ii) temperature, (iii) pressure and (iv) alkalinity. Therefore, a range of analytical techniques, as accurate as possible, are needed to understand the hydration reactions/processes. There are many techniques used for studying cement hydration and the most common ones were thoroughly treated in a book published in 2016 [3] which is the standard in the field.

Cement notation is used hereby. On the one hand, PCs have more than five crystalline components before water mixing: $C\underline{S}H_2$ (and/or other calcium sulfates), C_3S, C_3A, C_4AF, C_2S, ordered by their hydration kinetics in commercial PCs. On the other hand, and after partial dissolution, transport of mass and supersaturation, interacting precipitation reactions take place over existing surfaces, i.e. heterogeneous nucleation, and within the capillary porosity, i.e. homogeneous nucleation. In this hydrating environment, more than four new hydration products are formed: crystalline ettringite (AFt), nanocrystalline calcium silicate hydrate (C-S-H gel), crystalline portlandite (CH) and amorphous iron-siliceous hydrogarnet. Other hydrates can crystallize like AFm-type (sulfate, hemicarbonate, monocarbonate) depending upon the sulfate balance, etc. In PC blends containing supplementary cementitious materials (SCMs), there are even more hydrates, but this is not the focus of the present investigation.

Nowadays, the faithful time-dependent quantification of the components for neat PC hydration is relatively well-established [3]. This is still not the case for PC-SCMs blends where the degree of hydration of the SCMs is still not routinely obtained accurately by easy-to-automatize techniques. Moreover, the accurate analysis of the unaltered microstructures, at the different length scales, is still not well-established neither in PCs nor in PC-SCMs binders. This investigation focuses on the *in situ* analysis of PC hydration by combining two laboratory X-ray techniques, X-ray powder diffraction and X-ray microtomography (μCT), to contribute to help fill this scientific gap. It is noted that μCT was not covered in [3].

On the one hand and after decades of research, the quantitative phase analysis of crystalline components in hydrating PCs by laboratory X-ray powder diffraction (LXRPD) is well-established [4–8]. Moreover, the overall amorphous content may be obtained by using external [9] or internal [10] standard methodologies. These approaches have advantages and disadvantages, but this analysis is out of the scope of the present work. On the other hand and after about fifteen years of research, the quantitative analysis of the hydrating components and microstructures by μCT [11] is still challenging. The uses of μCT in cements have been reviewed [12–17]. The readers are referred to these works for knowing the features that can be followed and, in some cases, quantified.

This work is part of a long-term endeavour devoted to better understanding the development of the components and microstructures in cementitious materials by using techniques that do not require sample conditioning and where the data analysis can be automatized. To that end and in an initial work, laboratory X-ray powder diffraction and X-ray imaging were employed to analyse the same PC paste-filled capillary [18]. However, this work did not carry out any *in situ* hydration study. The PC hydration at early ages has been very recently *in situ* investigated by ptychographic synchrotron nanotomography [19] and the spatial dissolution rate of alite was reported. However, the access to this technique is not straightforward and the capillaries must currently have a maximum diameter of 200 μm to access nanoimaging spatial resolution. On the one hand, it must be clarified that the spatial resolution achieved with this technique, ~250 nm, is much better than the spatial resolution that can be attained using laboratory-based μCT, i.e. 2-3 μm. On the other hand, the availability and accessibility of ptychographic synchrotron nanotomography is very limited. Here, we report the combined use of LXRPD and laboratory μCT for studying the hydration of a PC paste. The reported approach avoids any sample conditioning step that could alter the samples/microstructures. A small fraction of this work has been accepted as a proceeding of the 16th International Congress on the Chemistry of Cement, 2023 [20]. Additional samples have been (*ex situ*) prepared here by well-established methodologies to assay the accuracy of the obtained results. These additional samples are investigated by thermal analysis, LXRPD and calorimetry. It is demonstrated that the proposed *in situ* methodology is accurate. This is a first, necessary, step before extending

82 this methodology to more challenging hydrating binders like PC-SCMs blends. The final aim is to be able to
83 determine the SCMs degree of reaction from this combination of techniques.

2. Materials and Methods

2.1. The Portland cement and its initial characterization.

86 A commercial Portland Cement type CEM I 42.5 R, conforming to EN 197–1, has been used. Its elemental
87 analysis by X-ray fluorescence (XRF) and its mineralogical analysis determined by Rietveld quantitative phase
88 analysis and thermal analysis are given in Table 1. The textural properties were also measured. The air
89 permeability, i.e. Blaine, value was 3750 cm^2/g. The specific surface area, measured by nitrogen isotherm with
90 an ASAP 2420 (Micromeritics, USA) instrument, and the density determined by He pycnometry using a helium
91 Pycnometer (Accupyc II 1320 Pycnometer, Micromeritics) equipped with a chamber of 10 cm^3, were 1.9 m^2g^{-1}
92 and 3.09 gcm^{-3}. Fig. 1 displays its particle size distribution as measured by laser diffraction in a Mastersizer
93 3000 device (Malvern Panalytical) by employing the Aero S dry chamber. $D_{v,10}$, $D_{v,50}$ and $D_{v,90}$ values were
94 2.0, 17.6 and 59.1 μm, respectively.

Table 1

96 Chemical (elemental) analysis (by XRF) and Rietveld quantitative phase analysis (by LXRPD) of the
97 employed Portland cement. All data are expressed in weight percentages.

chemical composition from XRF (wt%)		mineralogical composition from LXRPD (wt%)	
CaO	61.4	C_3S	58.3
SiO_2	19.9	β-C_2S	12.9
Al_2O_3	4.56	C_3A	6.7
Fe_2O_3	3.3	C_4AF	10.3
SO_3	3.9	$C\underline{S}H_{0.5}$	3.1
MgO	1.5	$C\underline{S}H_2$	2.2
K_2O	1.14	$C\underline{C}$	5.3
Na_2O	0.24	Minors	1.2
Others	0.4		
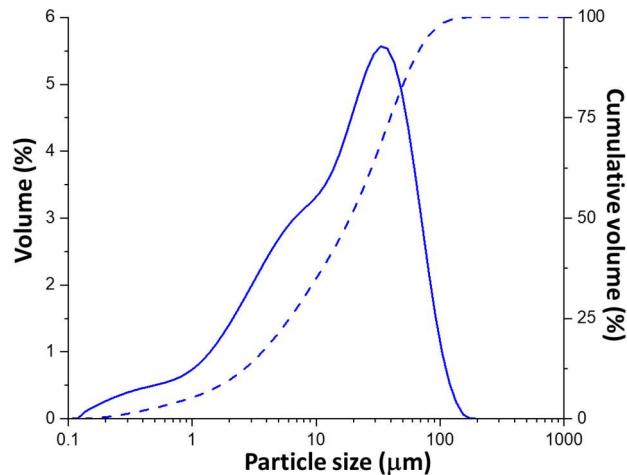
Figure 1. Particle size distribution (left – relative volume percentages, right – cumulative volume) determined by laser
101 diffraction for the anhydrous PC.

2.2. Paste preparation.

103 The pastes, for all the employed techniques, were prepared in exactly the same way. 50 g of PC and 25 g of
104 twice boiled distilled water were mixed, w/c=0.50, by mechanical stirring at 800 rpm for 90 s. After a resting
105 period of 30 s, the same stirring step was repeated. The water was boiled to remove the dissolved CO_2 and it
106 was cooled to 25 ºC, covered with a plastic film to avoid CO_2 diffusion. The resulting homogeneous paste was
107 used for filling three type of holders. A) For the *in situ* LXRPD and μCT studies, the paste was injected into a
108 glass tube with a nominal diameter of 2.0 mm using a syringe. Then, both ends were sealed with ultraviolet

3

(UV) curing adhesive to avoid any water loss and carbonation. B) For the *ex situ* diffraction and thermal studies, the paste was poured into polytetrafluoroethylene (PTFE) cylindrical moulds (length: 35 mm, diameter: 10 mm) sealed and rotated at 16 rpm for 24 hours at 25°C as previously reported [21,22]. After 1 day, the cylinders were demoulded and stored at 25°C for 6 additional days within (1) a plastic bottle filled with $Ca(OH)_2$-saturated water, and (2) a sealed plastic bag. The bottle was tightly closed to prevent carbonation and the volume of water was kept to a minimum to minimise any leaching. The samples were prepared just by gentle grinding in an agate mortar and the powder diffraction and thermal analyses were performed in those powders. C) For the calorimetric study, the paste was poured into the glass ampoule of the calorimeter. Table 2 lists the techniques and the samples used in this study.

2.3. Isothermal calorimetry.

This study was carried out by employing an eight-channel Thermal Activity Monitor (TAM) microcalorimeter from TA Instruments. The data were acquired at 25°C for a week. The first 45 minutes were not collected as this time was needed for the thermal stabilisation of the equipment. The selected temperature was dictated by the temperature of the X-ray laboratory room where the *in situ* studies were carried out.

2.4. Thermal analysis.

Thermogravimetric (TGA) traces for the two *ex situ* prepared samples, see Table 1, were recorded in an SDT-Q600 analyser from TA instruments (New Castle, DE, USA). The temperature was increased from 25 to 1000°C, with a 10 °Cmin^{-1} rate. The powders were loaded in open platinum crucibles and the experiment was carried out under synthetic air with a gas flow rate of 100 ml/min.

Table 2

Analytical techniques and paste preparation, always w/c=0.50, and holders employed in this study. The abbreviations for fabricated pastes are also detailed.

| technique	paste	*procedure*	*age*
μCT	within 2 mm glass capillary	*in situ*	12h, 1d, 3d, 7d, 79d
Mo-LXRPD	within 2 mm glass capillary abbreviation: **insitu-paste**	*in situ*	1d (27.5h), 3d, 7d, 77d
Calorimetry	within glass ampoule	*in situ*	continuous for 1 week
Mo-LXRPD, TA	Cylindrical paste cured in a sealed bag; abbreviation: **s.b.-paste**	*ex situ*	7d
Mo-LXRPD, TA	Cylindrical paste cured within CH-saturated water; abbreviation: **CH-paste**	*ex situ*	7d

2.5. Laboratory X-ray powder diffraction (LXRPD).

The X-ray powder diffraction study of the pastes was carried out by using a D8 ADVANCE (Bruker AXS) diffractometer at SCAI, University of Malaga (UMA), Spain. This diffractometer employs a Molybdenum anode and it has a monochromator to remove the Mo-Kα_2 radiation, yielding monochromatic Mo-Kα_1 X-rays (λ=0.7093 Å). The tube worked at 50 kV and 50 mA. The optical setup in both studies (*in situ* and *ex situ*) consisted of a primary monochromator, a focusing mirror, 2 mm anti-scattering slit and 2.5 Soller slits for the incident and transmitted beams. The X-ray detector was an EIGER from DECTRIS, Baden, Switzerland, optimised for Mo radiation, and operated with an aperture of 7×21 degrees. All powder patterns have been taken in transmission configuration, which minimises preferred orientation, with rotating samples (10 rpm), which maximises the random arrangement of the particles within the beam. High energy Molybdenum radiation is critical to *in situ* measure the diffraction signal of the pastes within glass capillaries of 2 mm of diameter. Cu radiation cannot analyse such thick capillaries as absorption is too high. As it will be shown in results section, this wide capillary is in turn needed to avoid self-desiccation at hydration ages later than one week.

For the *ex situ* studies, the pastes were loaded between two Kapton foils, without pressing. These powder were prepared as cylinders, as indicated in subsection 2.2, and just grinded. The patterns were collected in coupled 2theta/theta mode between 3 to 40° (2θ) counting for 101 min. The detector worked in VDO (Virtual Detector Opening) mode. For the *in situ* study, the paste within the glass capillary was mounted in a goniometer head, see Fig. 2, for alignment. The patterns were collected in decoupled 2theta mode between 1 to 38° (2θ) counting for 188 min. The detector worked in NOUT (No Over-/UnderTravel) mode. The *in situ* powder diffraction

patterns were collected just after the µCT data acquisition. Moreover, because in this study it is crucial to easily exchange between LXRPD and µCT, an additional piece has been designed which allowed using of a similar setup for the µCT to be able to scan the same volume of the capillary with time. This brass holder, which allows precise vertical positioning of the glass tube in the µCT, is displayed in Fig. 3. The powder patterns were taken at the ages indicated in Table 2.
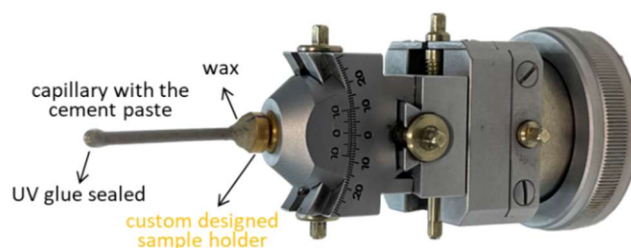
Figure 2. LXRPD setup for the *in situ* paste data collection.
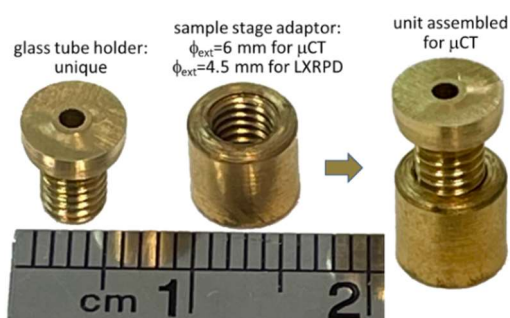
Figure 3. Custom designed sample holder for the *in situ* capillary alignment to scan the same volume with time.

The LXRPD data analysis was carried out by the Rietveld method. This was done by using the GSAS software [23] with an asymmetry-corrected pseudo-Voigt peak shape function [24,25]. The optimised overall parameters were: background coefficients, zero-shift error, phase scale factors, unit cell parameters, peak shape parameters, and preferred orientation coefficient if needed. The crystal structures used are described elsewhere [26,27] and they are explicitly given in Table 3.

Table 3

Crystal structures used in the Rietveld quantitative phase analysis including the ICSD code numbers.

| phase	ICSD code	reference
C_3S-M3	94742	[28]
β-C_2S	81096	[29]
o-C_3A	100220	[30]
C_4AF	9197	[31]
$C\underline{S}H_{0.5}$	151692	[32]
$C\underline{S}H_2$	151692	[33]
$C\underline{C}$	79528	[34]
Qz	41414	[35]
AFt	155395	[36]
CH	202220	[37]
Hc	263124	[38]

2.6. Laboratory X-ray computed microtomography (µCT).

The µCT datasets were acquired on a SKYSCAN 2214 scanner from Bruker at SCAI in the University of Malaga. Scans were obtained with an X-ray tube using a LaB_6 source (operated at 55 kV and 130 mA) and employing a 0.25 mm Al foil, between the sample and the CCD detector, to reduce beam hardening. After careful sample positioning and alignment, the capillary was rotated 360° during data acquisition. Images were taken every 0.2º, i.e. 1801 projections, with an exposure time of 1.9 s resulting in an overall recording time of 225 min per scan. The geometrical settings were a sample-to-source distance of 9.953 mm and a sample-to-

174 detector distance of 305.496 mm, see Fig.4. The CCD detector has a (physical) pixel size of 17.4 μm (binning
175 2×2). This pixel size and binning, together with the geometric setting, resulted in a voxel size of 1.1 μm. In
176 these conditions, the field of view was 2.2 mm horizontal and 1.5 mm vertical. With this experimental
177 configuration, the average X-ray transmission was about 55%. Objective lenses were not employed, and
178 therefore, the magnification was achieved using just the conical beam geometry.

179 The images were reconstructed using a cylindrical VOI (volume of interest) of 2.0×1.1 mm (H×V) using the
180 software NRecon (version 2.1.0.1, Bruker, Billerica, Massachusetts, United States). The reconstruction details
181 were: (a) beam hardening correction (%)=30; (b) smoothing=1 with smoothing kernel=2 (Gaussian), (c)
182 minimum for CS (cross section) to image conversion=-0.04 and (d) maximum for CS to image conversion=0.7.
183 Each reconstructed dataset has a 7 GB size (as 16-bit data). Flat-field corrections were applied for dark and
184 bright fields just before every scans. For *in situ* studies, an overall recording time not too high is mandatory.
185 NRecon software allows to use a smooth filter before the reconstruction of the data in order to increase the
186 signal-to-noise ratio, for the chosen recording conditions, which also reduces the data size.

187 Data analysis was carried out in two ways. Firstly, Dragonfly software (version 2022.1 for Windows™, Object
188 Research Systems (ORS) Inc., Montreal, Canada) was employed to segment the data based on global
189 thresholding. The intervals were determined as described in the results section. Secondly, IPSDK Explorer
190 program (version 3.2.0.0 for Windows™, Reactiv'IP, Grenoble, France), was used for a supervised machine
191 learning (ML) image analysis [19]. 4D rendered volumes, showing the results of both approaches, were
192 visualised with Dragonfly.

193 Machine learning for microstructural characterization of cementitious materials has been currently reviewed
194 [39] and an analysis of different methodologies/algorithms is out of the scope of the present investigation. A
195 software based on random forest approach was chosen based on its simplicity and lower parameterisation
196 requirements. Unlike more complicated algorithms such as neural networks, which can be quite parameter-
197 dependent and computationally expensive, the random forest approach is relatively easy to build and
198 computationally efficient. It requires minimal modification, especially in the number of trees, making it a
199 viable option for this application. Moreover, this software does not require Graphics Processing Unit (GPU).
200 Softwares requiring GPU are more powerful but they may also have compatibility issues between the
201 computer(s) and the software needing tailored-PC configurations, i.e. no compatible with other softwares.
202 Concerning the features used in the algorithm, they are computed by using the pixel neighbourhood, so it is
203 not limited only to the pixel value, like the global thresholding approach. Direct clustering methods like k-
204 means and self-organizing maps [39] have not been tried as the primary target has been to use an alternative
205 supervised ML approach to the global threshold method.
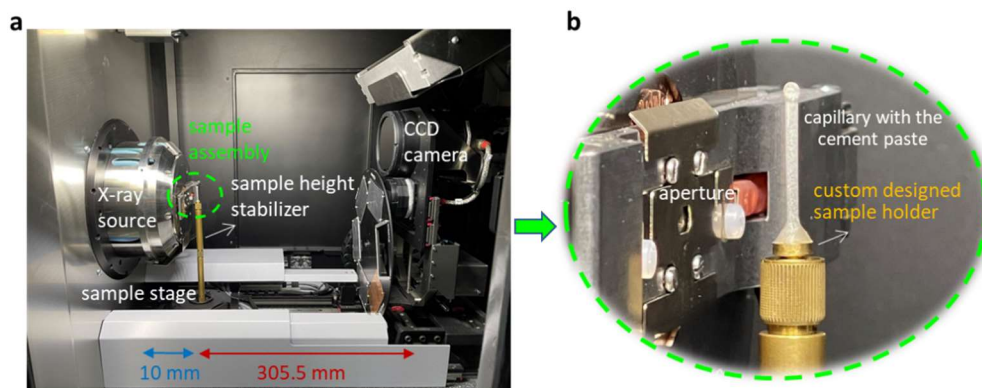
206

207   **Figure 4.** Laboratory μCT setup for the *in situ* paste data collection. (a) General view. (b) Capillary detailed view.

208 **3. Results and discussion.**

209 The main objective of this work is to evaluate the PC paste hydration without sample conditioning and to
210 evaluate the accuracy of the resulting analyses. In order to do so, in addition to the central *in situ* study, well-
211 established *ex situ* studies have been also carried out to have reference values. With this approach, additional
212 values can be obtained, like the key portlandite content.

213 **3.1. *Ex situ* thermal analysis study.** Fig. 5 displays the thermal traces for the two pastes hydrated in a
214 portlandite saturated solution and in a sealed bag. The employed PC has 5.3 wt% of calcite that corresponds

to 3.53 wt% in the resulting pastes. Because calcite losses 43.9% mass on heating due to the CO_2 release, the expected mass loss due to the initial calcite content is 1.55%. The mass losses in the calcite temperature decomposition interval were 1.87% and 1.57% for the s.b.-paste and CH-paste, respectively. Therefore, carbonation of the pastes is not significant. Moreover, the total expected weight loss is derived from the added water 33.33% and from the initial anhydrous cement components (mainly calcite and gypsum). The calculated, i.e. expected, overall weight loss is 35.32 wt%. The measured weight losses are 35.1 and 35.2% for s.b.-paste and CH-paste, respectively. This indicates: (a) very minor water loss during the gentle grinding prior to the thermal analysis, and (b) a very robust and accurate experimental procedure.

If carbonation is negligible and the experimental procedure is robust and accurate, it is possible to trust in the direct portlandite contents derived from the weight losses in the portlandite decomposition temperature interval, see Fig. 5. The measured weight losses are 3.5 and 3.2% for s.b.-paste and CH-paste, respectively. Thus, the portlandite contents are 14.5 and 13.1 wt% for s.b.-paste and CH-paste, respectively, referred to 100 g of cement paste. The average value, 13.8 wt% of CH at 7 days of hydration, will be the reference for the *ex situ* and *in situ* quantitative phase analyses derived from the powder diffraction data.
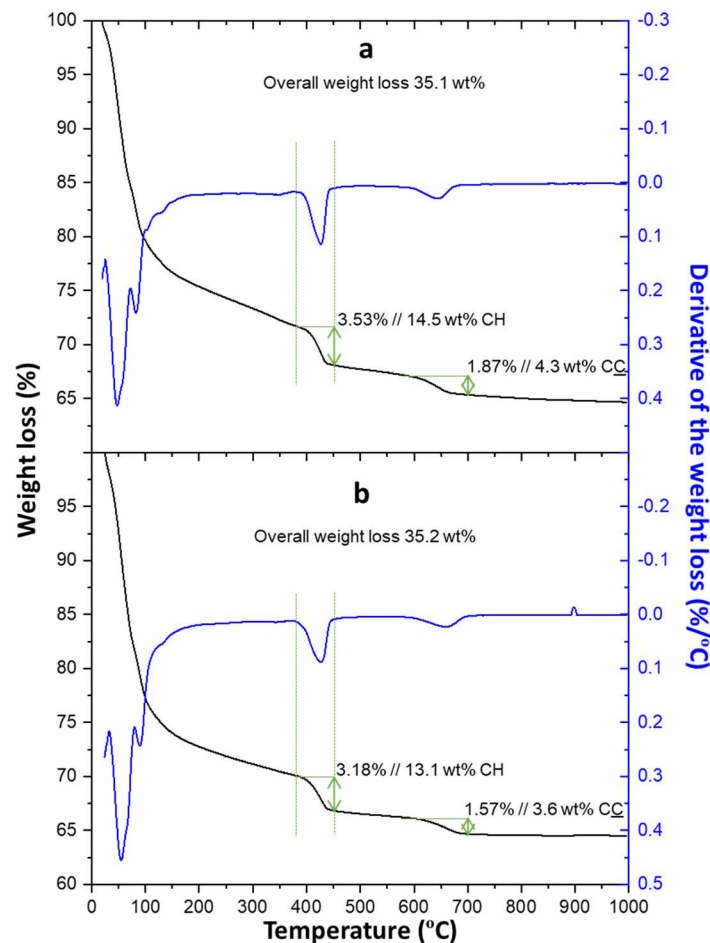
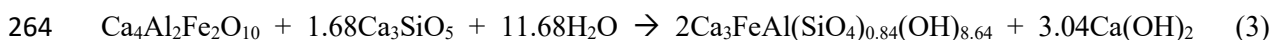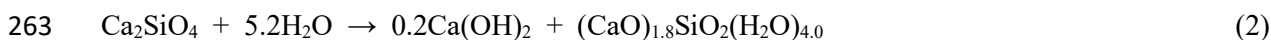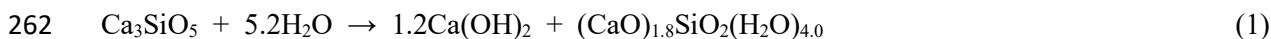**Figure 5.** Thermal analysis traces for the studied pastes. **(a)** PC-paste hydrated for 1 day within the PTFE mould and then 6 additional days within the sealed bag (s.b.-paste). **(b)** PC-paste hydrated for 1 day within the PTFE mould and then 6 additional days within a CH-saturated solution (CH-paste).

3.2. *Ex situ* laboratory X-ray powder diffraction study.

The $MoK\alpha_1$ powder patterns were analysed by the Rietveld method as detailed above. The Rietveld quantitative phase analysis (RQPA) outputs, direct results, are referred to 100% of crystalline phases and they are given in Table 4 and the fits are displayed in Fig. 6. These numbers are quite similar, for the two sample hydration conditions, showing the robustness of the overall employed methodology (i.e. experimental and data analysis). Moreover, and as expected, the reactivities are slightly larger when cured under CH-saturated water. However, the reported numbers do not consider the free water or any amorphous content including the C-S-H amount. In order to make comparisons, these values should be referred to a constant basis. The most used bases in cement studies are 100 g of anhydrous cement or 100 g of cement paste. Our research group always refers

the results to 100 g of cement paste for direct comparison to any other cement paste measurement including the thermal analysis outputs. Of course, when referred to a constant basis, the calculation of the degree of hydration of every phase is straightforward.

Here, mass balance calculations have been carried out to refer the results to 100 g of cement paste where some assumptions are carried out in order to estimate the amount of amorphous phases: (a) amorphous C-S-H gel is formed according to the hydration of C_3S following reaction (1) [40] with a C/S ratio of 1.80 and a water content of four molecules per SiO_2 mol. With these assumptions, every gram of reacted C_3S consumes 0.408 g of water and produces 0.388 g or portlandite and 1.020 g of C-S-H gel; (b) belite hydration is negligible in the first week, and hence it does not produce further C-S-H gel. If belite reacts at later ages, the assumed stoichiometries are given in reaction (2). Hence, every gram of reacted C_2S consumes 0.438 g of water and produces 0.086 g or portlandite and 1.352 g of C-S-H gel; (c) ferrite in the presence of alite is assumed to hydrate to give amorphous iron-siliceous hydrogarnet (Fe-Si-Hg) according to reaction (3) [41–43], where all aluminium is incorporated in the Fe-Si-Hg amorphous component. Every gram of reacted C_4AF consumes 0.789 g of C_3S and 0.433 g of water, and produces 0.463 g or portlandite and 1.352 g of Fe-Si-Hg gel; (d) C_3A in the presence of gypsum gives ettringite according to reaction (4). Every gram of reacted C_3A consumes 1.912 g of gypsum and 1.735 g of water, and produces 4.648 g or ettringite; (e) the formation of any amorphous AFm type phase is not considered; and (f) the amount of free water is computed by removing the water content of the hydrated phases (crystalline and amorphous) from the initial water content, 33.33 g in 100 g of cement paste. It is explicitly stated that the stoichiometries of the amorphous compounds C-S-H gel and Fe-Si-Hg gel have been assumed.

$$Ca_3SiO_5 + 5.2H_2O \rightarrow 1.2Ca(OH)_2 + (CaO)_{1.8}SiO_2(H_2O)_{4.0} \tag{1}$$

$$Ca_2SiO_4 + 5.2H_2O \rightarrow 0.2Ca(OH)_2 + (CaO)_{1.8}SiO_2(H_2O)_{4.0} \tag{2}$$

$$Ca_4Al_2Fe_2O_{10} + 1.68Ca_3SiO_5 + 11.68H_2O \rightarrow 2Ca_3FeAl(SiO_4)_{0.84}(OH)_{8.64} + 3.04Ca(OH)_2 \tag{3}$$

$$Ca_3Al_2O_6 + 3\ CaSO_4{\cdot}2H_2O + 26H_2O \rightarrow Ca_6Al_2(SO_4)_3{\cdot}26H_2O \tag{4}$$

Table 4

Direct *ex situ* RQPA results (referred to 100% of crystalline phases) for the two studied PC pastes, w/c=0.50, expressed in wt%. Hc stands for hemicarboaluminate AFm phase.

phases	CH-paste	s.b.-paste
C_3S /wt%	9.6	12.0
C_2S /wt%	15.6	16.5
C_3A /wt%	0.8	0.7
C_4AF /wt%	10.1	10.0
C$\underline{C}$ /wt%	9.3	8.9
others /wt%	0.9	1.0
AFt /wt%	24.8	22.9
CH /wt%	28.2	27.2
Hc /wt%	0.8	0.9

Table 5 displays the RQPA results referred to 100 g of cement paste. The data at mixing correspond to the analysis of the anhydrous cement, reported in the experimental section, expressed in 100 g of cement paste containing 33.33 wt% of water, i.e. w/c=0.50. For the CH-paste and s.b.-paste, the amorphous phases are calculated according to the reactions given above. The assumptions seem to be close to correct as the resulting portlandite contents at 7 days of hydration are 13.2 and 12.9 wt% for CH-paste and s.b.-paste, respectively. These values agree relatively well with the values obtained from the thermal analysis study: 13.1 and 14.5 wt%, respectively. Moreover, the portlandite contents can be calculated from the reactivities of C_3S and C_4AF given in equations (1) and (3). The calculated CH amounts are 13.72 and 13.26 wt% for CH-paste and s.b.-paste, respectively. The good agreement between the portlandite content from these three approaches, (i) thermal analysis (13.8 wt%), (ii) measured RQPA (13.1 wt%), and (iii) calculated amount based on the clinker phase reactivities (13.5 wt%), shows the accuracy in this study and provides a reference value of the portlandite content at 7 days for the *in situ* study detailed below, i.e. 13.5 wt%. The derived degree of hydration (DoH) is totally in line with the known phase reactivities [1,2]. It is noted that neither the internal standard nor the external standard approaches have been used here to determine the overall amorphous phase content. Here,

mass balance calculations are employed to estimate the contents of the main amorphous phases based on the hydration reactions.
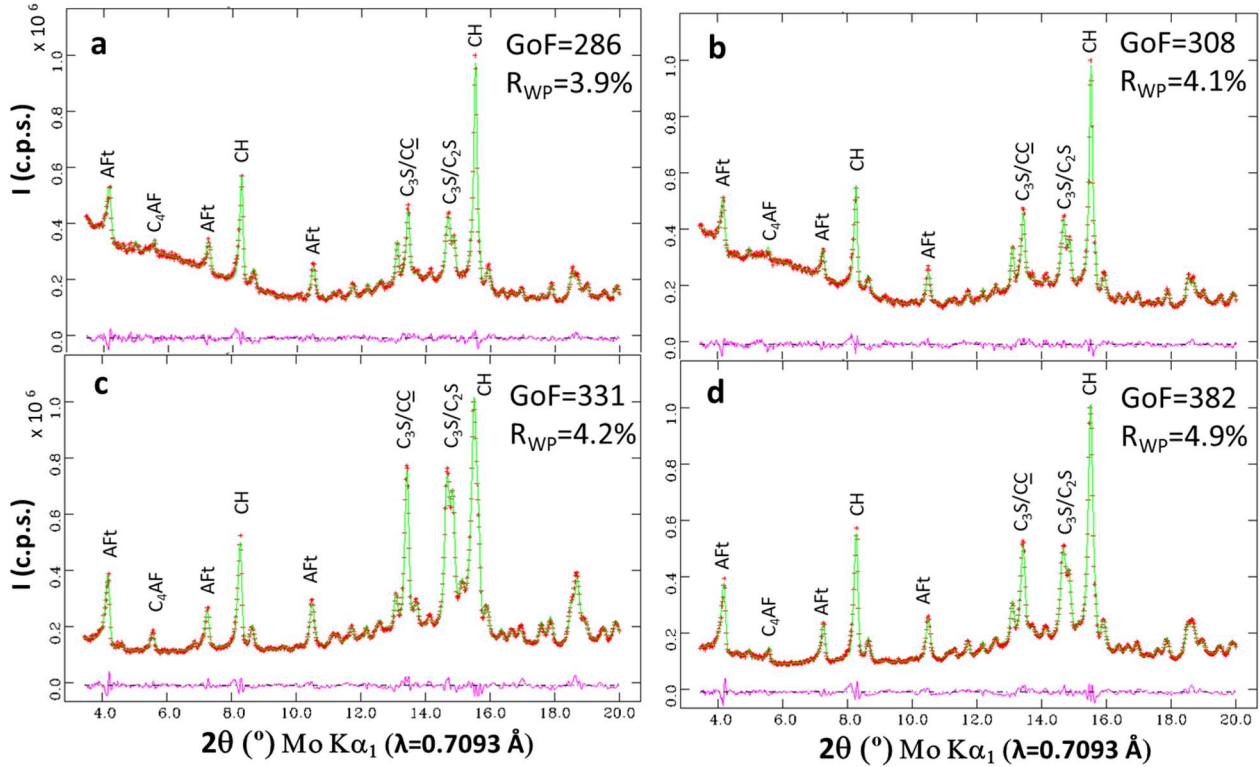
Figure 6. Mo-Kα_1 (λ=0.71 Å) Rietveld plots for **(a)** CH-paste hydrated for 7 days; **(b)** s.b.-paste hydrated for 7 days, **(c)** insitu-paste hydrated for 1 days; and **(d)** insitu-paste hydrated for 7 days.

Table 5

Ex situ and *in situ* RQPA results for PC 42.5 pastes, w/c=0.50, expressed in wt% and referred to 100 g of cement paste. The calculated contents (for the amorphous phases) are given in italics. The values of the factor needed to refer the crystalline contents (referred to 100% of crystalline material) to 100 g of cement paste are also given in bold and italics. The degree of hydration (DoH) of selected phases are also listed. Mc stands for monocarboaluminate (AFm type phase).

phases[#]	insitu-paste					CH-paste	s.b.-paste
	t_0	1d	3d	7d	77d	7d	7d
C_3S /wt%	38.9	15.3	7.5	6.2	4.1	4.5	5.7
C_2S /wt%	8.6	8.2	8.5	8.1	7.4	7.3	7.9
C_3A /wt%	4.5	2.1	1.0	0.5	0.3	0.4	0.3
C_4AF /wt%	6.9	6.2	4.6	4.4	3.7	4.7	4.8
C$\underline{C}$ /wt%	3.5	4.7	5.1	4.8	5.0	4.3	4.2
others /wt%	4.3	0.5	0.3	0.4	0.4	0.4	0.5
H_2O /wt%	33.3	*19.1*	*15.0*	*13.9*	*12.5*	*12.4*	*14.1*
AFt /wt%	-	9.0	10.2	10.7	11.0	11.6	10.9
CH /wt%	-	9.0	11.7	12.5	13.3	13.2	12.9
C-S-H /wt%	-	*24.7*	*32.1*	*34.0*	*36.1*	*37.0*	*34.5*
Fe-Si-Hg /wt%		*1.2*	*4.1*	*4.3*	*5.6*	*3.8*	*3.9*
Hc /wt%	-	-	0.2	0.2	0.1	0.4	0.4
Mc /wt%	-	-	-	-	0.6	-	-
factor	*0.667*	*0.549*	*0.489*	*0.478*	*0.458*	*0.468*	*0.476*
C_3S-DoH /%	-	61	81	84	89	88	85
C_3A-DoH /%	-	52	78	89	94	92	93
C_4AF-DoH /%	-	10	34	36	47	31	31

9

3.3. *In situ* laboratory X-ray powder diffraction study.

It is noted that the same PC paste has been analysed by *in situ* LXRPD and μCT. This reduces the variability in the studies as PCs are heterogeneous materials. The LXRPD data were analysed by the Rietveld method and the fits at 1 and 7 days, as examples, are also displayed in Fig. 6. The RQPA direct results, referred to 100 wt% of crystalline content, are given in Table 6. The data shown in Table 6 indicate that C_3S keeps reacting for up to 77 days. This is expected but previous results from our research group evidenced that PC hydration stops, for some pastes, as early as one week in capillaries of 1 mm or thinner [44]. This observation was variable because the water availability depends upon the initial w/c ratio but also upon the C_3S content and the amount of AFt formed at early ages. This behaviour was very likely due to self-drying but a thorough investigation to fully understand that feature has not been attempted. This research focuses on developing a robust and easy experimental method yielding accurate results. Hence, thick capillaries, 2 mm of diameter, have been employed in spite that this yields (slightly) poorer resolution in the LXRPD and μCT data. In any case, Table 6 also shows the *in situ* results for the same PC paste but within a capillary of 1.5 mm of nominal diameter. It is clear that the hydration reactions have (slightly) slowed down already at 7 days. The C_3S content is larger and chiefly, the CH content is lower.

The *in situ* RQPA direct results, listed in Table 6, have been referred to 100 g of cement paste and the values were reported in Table 5, together with the results from the *ex situ* LXRPD study for easy comparison. The previously reported reactions have been again considered to estimate the contents for the non-crystalline phases: C-S-H gel and Fe-Si-Hg. Moreover, and as indicated above, the free water content is estimated by the subtraction of the water contained in all (measured and calculated) hydrates from the added nominal amount of water. Several observations/conclusions can be drawn from the *in situ* RQPA data reported in Table 5:

(I) The experimental method is robust, and the data analysis seems to be accurate as the determined portlandite content at 7 days, i.e. 12.5 wt%, agrees very well with the data reported above for the same paste cured in different conditions, about 13.5 wt%. Moreover, mass balance calculations based on the reacted amounts of C_4AF and C_3S yield 13.1 wt%.

(II) The ettringite content keeps growing up to 77 days without any signature of decrease at later ages, which is in line with the high SO_3 content of the employed PC, i.e. 3.9 wt% (2.6 wt% referred to 100 g of cement paste). It is noted that in many cases inaccurate AFt contents are reported due to the employed hydration arresting procedure(s) [45–48]. The maximum amount of AFt, if all sulfates are incorporated within ettringite, would be 13.6 wt%. This value compares well with the measured one at 7 days, i.e. 10.7 wt%, as a fraction of the sulfates is incorporated/adsorbed in other phases, mainly amorphous ones like C-S-H gel and Fe-Si-Hg.

(III) As expected, the obtained contents for the different components at 7 days in the *in situ* study are slightly more similar to the 'sealed bag' results than to the 'CH cured' ones. See for instance the C_3S and free water contents in Table 5.

(IV) A minor carbonation is measured in the first analysis and subsequently, no further carbonation is observed.

(V) The renormalization factor to refer the contents to 100 g of cement paste, see Table 5, always decreases as the amount of amorphous phases invariably increases. This is the case in the hydration on neat PCs but this is not the case in the hydration of calcium sulfoaluminate cements but the extension of this methodology to those cements will be the subject of a forthcoming publication. Moreover, the evolution of total amorphous phases in PC-SCMs is at the core of a current investigation.

(VI) Finally, it is not ruled out that the *in situ* kinetics reported here are slightly slowed down at late ages due to partial self-desiccation. However, increasing the size of the capillary beyond 2 mm is currently judged to be unsatisfactory as the poorer spatial resolution in μCT and the larger peak overlapping in LXRPD which would yield less accurate results.

It is remarked here that avoiding carbonation and attaining robust results for AFt and CH are very useful outputs themselves, not to mention the combination with μCT results, see just below. Moreover, the addition of an internal standard is not needed for the reported methodology. The addition of a standard, with a small particle size to have random particle orientation, could affect the kinetics of the PC hydration reactions.

Table 6

Direct *in situ* RQPA results (referred to 100% of crystalline phases) for the PC paste, w/c=0.50 within a 2 mm capillary, expressed in wt%. Data at 7 days for the same PC paste but filled within a capillary of 1.5 mm of diameter are also given in italics.

phases	1d	3d	7d	7d (ϕ=1.5 mm)	77d
C_3S	27.8	15.3	13.0	*14.1*	9.0
C_2S	14.9	17.3	17.0	*15.7*	16.1
C_3A	3.9	2.0	1.0	*1.4*	0.6
C_4AF	11.2	9.3	9.2	*9.6*	8.0
C$\underline{C}$	8.6	10.4	10.0	*11.0*	10.9
others	0.9	0.6	0.8	*0.8*	0.8
AFt	16.3	20.9	22.3	*22.9*	24.0
CH	16.3	23.9	26.2	*23.8*	29.0
Hc	-	0.3	0.5	*0.5*	0.3
Mc	-	-	-	-	1.2

3.4. *In situ* laboratory X-ray computed microtomographic study.

μCT directly shows the dissolution of anhydrous phases, if there is enough contrast and spatial resolution. This is independent of the amorphous or crystalline nature of the imaged particles. Therefore, it is very complementary to LXRPD which is blind to the amorphous phase(s). Moreover, for *in situ* studies there is a strong constraint in the μCT data analysis as the particles/volumes of the anhydrous phases can only decrease. However, μCT is blind to the particles smaller than the true spatial resolution of the measurements, not the voxel size. In other words, if the spatial resolution of the measurements is 2.5 μm, the hydration of the particles with smaller spatial resolution cannot be directly followed. For decreasing the variability in the obtained results, the reported methodology proposes that the same region in the acquired μCT scans (i.e. data from exactly the same volume) is used for data analysis, including segmentation. To illustrate this, the same horizontal view of the cylindrical capillary paste studied at 12 hours and 1, 3, 7, and 79 days of hydration is shown in Fig. 7. The top row displays the full orthoslice and a magnified view of the same region is displayed in the bottom row. The preferential dissolution of the smallest cement grains at early ages (brightest particles) is readily visible as well as the paste densification. This second feature is evident from the evolution of the grey regions with time. It is explicitly stated that the μCT data were collected in 3 h and 45 min and this is quite long for pastes hydrating in the acceleration period or close to it, i.e. 12 h. However, the blurring because particle dissolution during the measurement is not large, see Fig. 7. The implication of this effect on the accuracy of the data is presently not established. On the other hand, synchrotron μCT can collect data with slightly better spatial resolution (and better contrast) in 5 to 10 minutes that can contribute to understand this effect. However, the availability of this technique is quite limited.
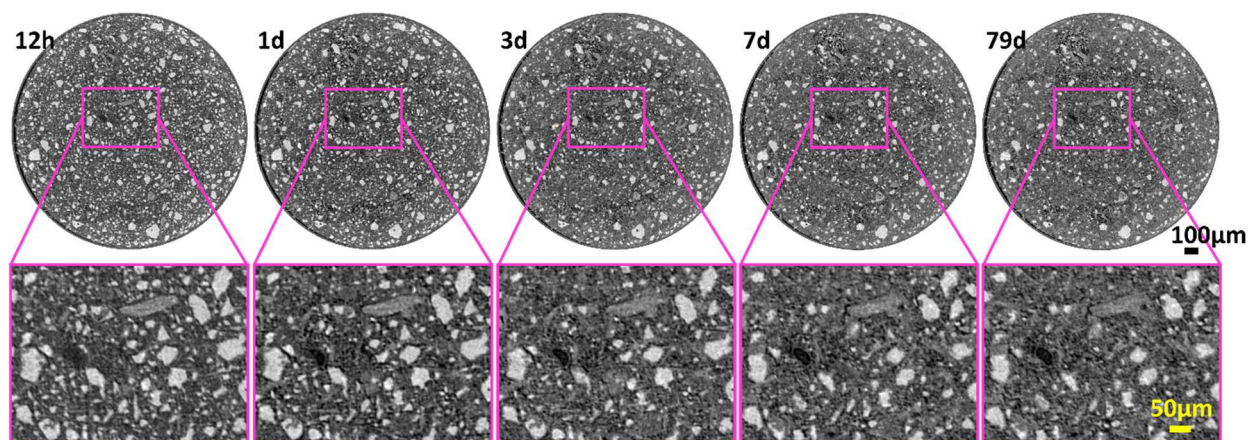

Figure 7. μCT orthoslices at the studied hydration ages. (Top row) full data evidencing the enhanced reactivity of small particles. (Bottom row) Same enlarged view to follow up the paste changes with hydration time.

11

Four types of regions can be observed in this type of laboratory study, which have different enough linear attenuation coefficients (LAC), and they are highlighted in Fig. 8. Firstly, the darkest regions are porosity, i.e. water and air. This X-ray imaging modality cannot distinguish air from water. Secondly, the darkest-grey volumes are labelled as low-density hydrated products (ld-HP) and these are the regions with lower grey-values. ld-HP should correspond mainly to C-S-H gel and AFt. Thirdly, the whitish-grey regions have higher LAC values and they are labelled as high-density hydrated products (hd-HP). These volumes should mainly correspond to CH, with a contribution of high-density C-S-H and calcium carbonate. Fourthly, unhydrated cement particles (UCP) are the white particles and they correspond to C_2S, C_3S, C_4AF and any remaining C_3A.

Pixel size is related, but it does not equal, to the spatial resolution in the µCTs. There is not a universal approach to measure the resolution in a given tomogram. Here, the edge sharpness across selected interfaces has been used to characterise the spatial resolution. ISO/TS 24597 defines the Gaussian radius of the point spread function of the images as the resolution, which is the change between 25%–75% grey value across the interfaces [19,49,50]. This approach, applied to the interface of the capillary outer wall [19], gave 2.3(6) µm from 10 measurements. This type of plot, for a pore of the paste, is shown in the right panel of Fig. 8. The derived spatial resolution is similar, ~2.8 µm. This value for the resolution is in line with previous investigations where it was reported that spatial resolution is generally 2-3 times poorer than the voxel size. The main consequence of the attained spatial resolution, about 2.5 ~µm, is that the particles with that overall size (or smaller) cannot be identified. They are accounted within the nearby component which is likely the most abundant one, the i.e. the hydrate phases intermixed with the capillary water. As it will be discussed later, this effect leads to a slight overestimation of the hydrated products (HP) and a small underestimation of the unhydrated cement particles (UCP). Every strategy to improve the spatial resolution (and the contrast) is highly desirable as it will lead to better analyses.
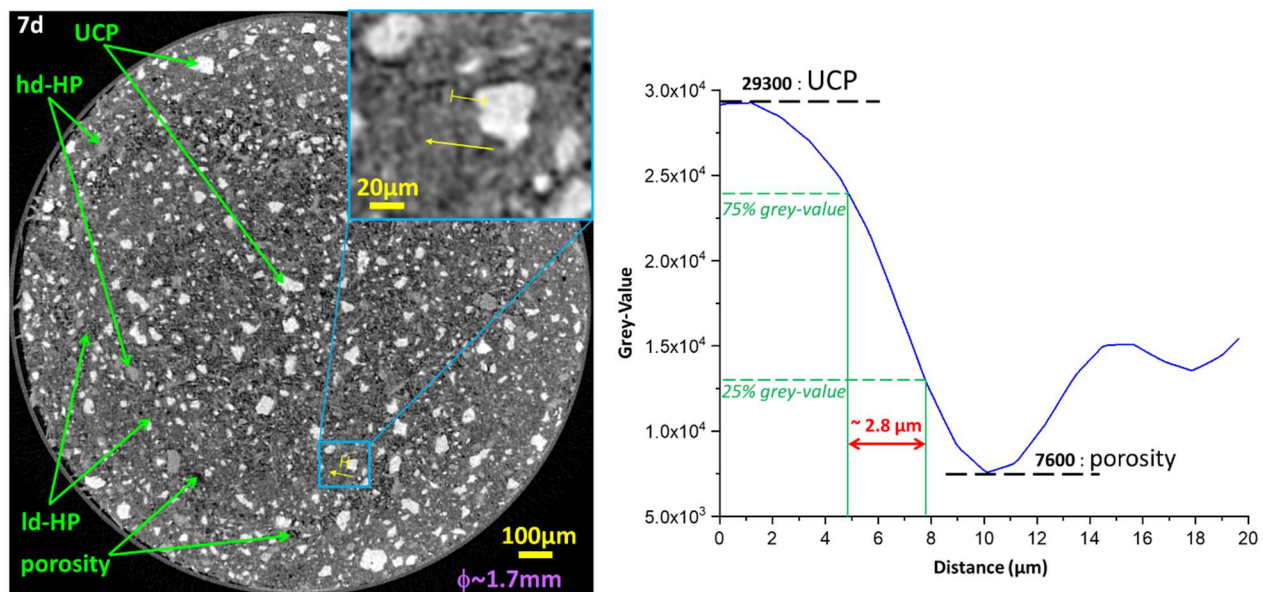
Figure 8. µCT orthoslice where the different components that can be visualized are highlighted: porosity, low-density hydrated products (ld-HP), high-density hydrated products (hd-HP) and unhydrated cement particles (UCP). The spatial resolution can be estimated from the line plot shown in the left panel (yellow line) and the corresponding grey-value profile shown in the right panel, see the text for details.

A first semiquantitative study can be carried out by inspecting the time evolution of the grey-value histograms for exactly the same hydrating volume, see Fig. 9. Several features were observed which deserve discussion:
(I) The employed experimental conditions allow the separation of the UCP from the HP, for particles larger than the attained spatial resolution. However, this does not preclude the existence of partial volume effects. This is unavoidable in cement binders where the size of many particles is smaller than the spatial resolution of the measurements [51].
(II) As expected, the amount of UCP decreases with time and the amount of HP increases, see red arrows. Moreover, it is worth noting that the number of voxels at ~22000 grey-value (i.e. right-tail of the HP peak) decreases with time which is a firm evidence that this is mainly due to UCP.

409 (III) There is a constant crossing point at ~20500 grey-value for the employed experimental conditions, see
410 black arrow in Fig. 9. From the time evolution, it is clear that particles with grey values above this number are
411 mainly UCP and particles with grey values below this number are mainly HP.
412 (IV) Densification of HP is evident as the maximum of the HP not only increased, but it is smoothly moved
413 towards larger grey values (see red arrow at the top).
414 (V) High-density and low-density HP cannot be distinguished in the histograms very likely due to the fine
415 intermixing of the particles in the paste.
416 (VI) The signature of air porosity development, i.e. shrinkage, is evident in the left-tails of the HP, see Fig. 9.
417 In spite of water consumption and binder densification (movement of the HP towards larger grey-values), the
418 number of voxels in the left-tails at ~6000-8000 grey-value, increases with time because the development of
419 air, i.e. liquid-water empty, porosity.
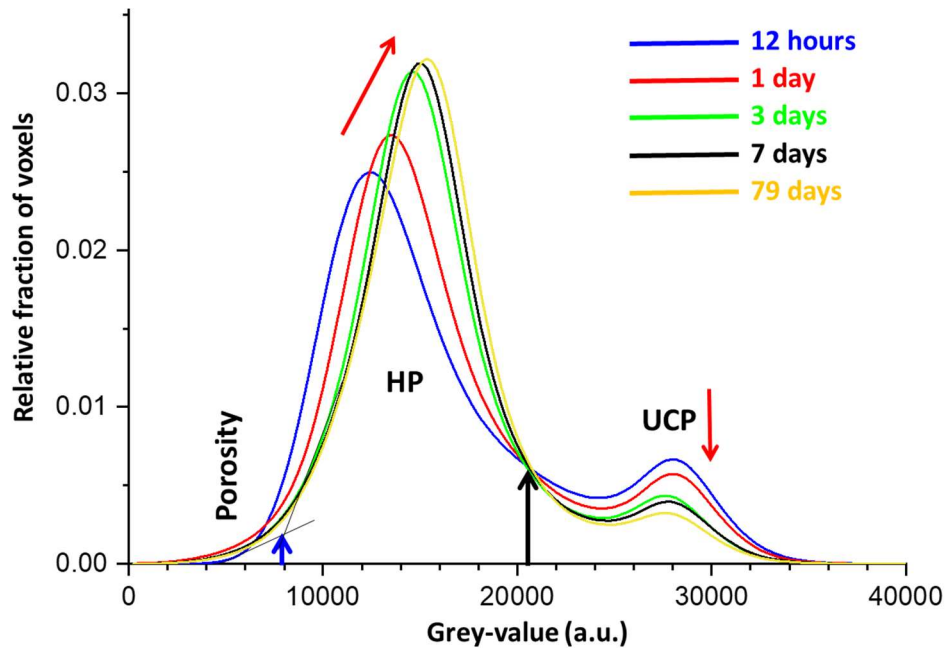
Figure 9. Time evolution of the grey-value histograms showing the evolution of the different components. For the description of the labels, see the text.

423 Quantitative analysis of the tomograms can be derived from their segmentations, in other words, the
424 quantitative classification of the different components that can be disentangled. The analysed VOI, ~1.4 mm³,
425 was a cylinder with a height of ~0.6 mm, and a diameter of ~1.7 mm, see Fig.10. This ensures a sufficiently
426 large volume which should not produce any bias because of insufficient averaging. This VOI is the
427 superimposed region inside the capillary that was imaged at each of the 5 hydration ages and it is significantly
428 smaller than the reconstructed VOI for each acquisition, ~4 mm³. Here, the segmentations have been carried
429 out by two approaches: global thresholding (GT) and Machine Learning (ML). Next, we focus on the GT
430 which only uses the information available in the grey-value histograms. Dragonfly was employed for this and
431 only three components were segmented: UCP, HP and porosity. The grey-value for the UCP/HP boundary is
432 constant with time, being 20500 grey-value for the employed experimental conditions and reconstruction
433 parameters. Conversely, the HP/porosity boundary is not constant with time and it was estimated for every
434 dataset by the tangent-slope approach [43]. The values ranged 6000-8500 grey-value and the estimation for
435 the 7 days tomogram is depicted in Fig. 9, as an example. The volume percentages of the three components
436 for the *in situ* μCT study are given in Table 7. The time evolution follows the expected trend, a decrease in the
437 UCP contents and an increase in the HP amounts. However, the accuracy of the obtained results required a
438 comparison with expected values which will be carried out below.

439 ML segmentation was carried out with IPSDK software employing the random forest approach. The ML model
440 training for PC pastes, including the initial pixel labelling and tweaking the model was described elsewhere
441 [19]. It is noted that for this type of analysis, four components were assigned: porosity, ld-HP, hd-HP and UCP.
442 ML profits not only from the grey-values but also from the local features of the (initially) manually labelled
443 particles. It is noted that the (supervised) training of the model is operator dependent, and therefore the
444 replicability is challenging. The results from this study are given in Table 8. It should be noted that the porosity

is always much smaller than the expected one. For instance, the free water content at 1 day from diffraction should be close to 36 vol% (19.1 wt%, see Table 5). Most of the water porosity is smaller than the attained spatial resolution, ~2.5 µm, and it is concluded that (a) the porosity values shown in Tables 7 and 8 are mainly air porosities, and (b) the free water is manly considered within the HP contribution. A 4D visualization of the ML segmentations is shown in Fig. 10.

Table 7

µCT global-thresholding segmentation results, in volume percentage (vol%).

time	porosity	HP	UCP
12 h	0.8%	76.6%	22.6%
1 d	2.6%	77.8%	19.6%
3 d	4.1%	80.6%	15.3%
7 d	2.4%	82.8%	14.8%
79 d	2.6%	84.3%	13.1%
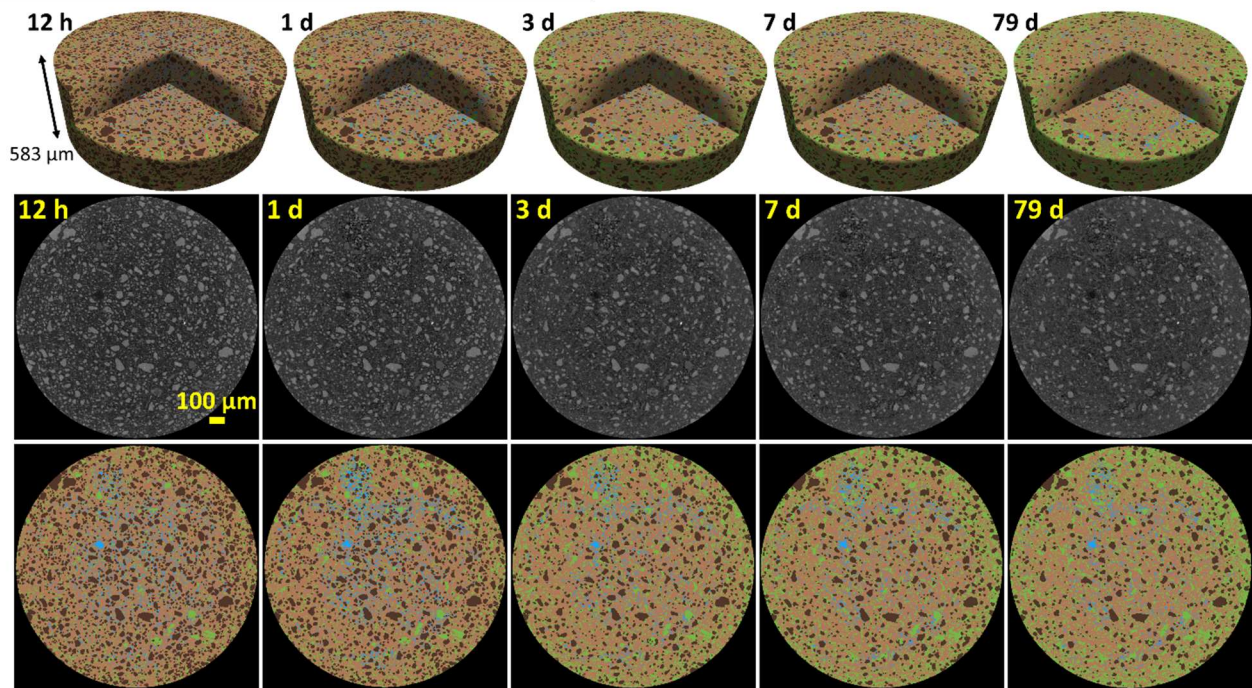
Figure 10. µCT Machine Learning segmentation output. (Top row) 4D renderings. Colour code: porosity (pale blue), low-density HP (light brown), high-density HP (green), unhydrated cement particles (dark brown). (Bottom row) 2D comparison of the reconstructed orthoslices and the ML segmented output.

Table 8.

µCT machine learning segmentation result, in volume percentage (vol%).

time	porosity	ld-HP	hd-HP	UCP
12 h	4.1%	55.8%	12.6%	27.5%
1 d	4.4%	56.6%	16.2%	22.8%
3 d	3.3%	57.9%	22.6%	16.2%
7 d	3.1%	56.3%	25.3%	15.3%
79 d	2.9%	55.5%	29.1%	12.5%

3.5. *In situ* isothermal calorimetric study.

The hydration kinetic of the employed PC has also been investigated by isothermal calorimetry, see Fig. 11. The maximum in the heat flow trace took place at 8 h. From the cumulative heat trace is deduced that the released heat at 27.5 hours, 3 and 7 days of hydration are 209.6, 295.7 and 325.1 J/g of anhydrous cement, respectively. From the RQPA results, it is possible to calculate the expected heat released considering the reaction degree of the different phases and their heats of hydration. For a detailed explanation, see [52]. Here, it is used 517, 1672 and 418 J/g for the heat of hydration of C_3S, C_3A (to yield AFt) and C_4AF, respectively.

For this comparison, the basis is 1 g of anhydrous cement. Therefore, the reacted amount of these phases has to be referred to 1 g of anhydrous PC and then the heats of hydration are used.

Following this approach, the calculated heats of hydration, from the RQPA-determined reacted fractions, are 247.5, 345.5 and 369.4 J/g at 27.5 h, 3 and 7 days, respectively. It can be noticed that the calculated heats are invariably higher than those directly measured by calorimetry. There are two main sources of error for this type of comparison: (i) Firstly, lower heats are measured by calorimetry because the data during the first 45 minutes were not collected, due to the needed thermal stabilization of equipment. (ii) Secondly, not all C_3A hydrates yield AFt because of the lack of sulfates. In fact, the reacted amount of C_3A at 7 days, i.e. 4.0 g, should yield 18.6 g of AFt. In fact, only 56% of the reacted C_3A gives AFt. Crystalline sulfate-containing AFm has not been detected in any diffraction study, the heat of hydration for this reaction would be 1144 J/g. Additionally, the heats of hydration of C_3A to yield aluminates adsorbed in the amorphous components and amorphous AFm are not known to the authors. 44% of C_3A, not yielding AFt, rests 19.6 J, and this is judged as the largest source of error for this comparison.
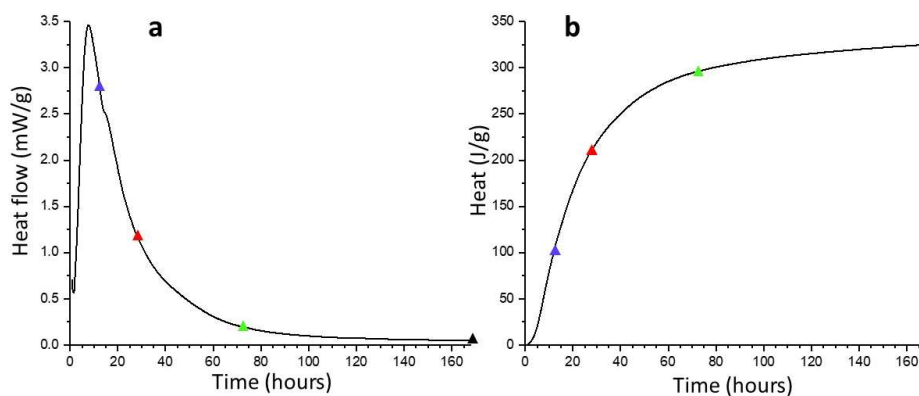
Figure 11. Isothermal calorimetry traces for the PC paste, w/c=0.50, at 25ºC up to 7 days. (a) Heat flow. (b) Cumulative heat. The triangles highlight the times for µCT or LXRPD data acquisitions. Blue: µCT recorded at 12 h. Red: LXRPD recorded at 27.5 h. Green and black: data acquired at 3 and 7 days, respectively.

4. General discussion.

The core of this investigation is to develop a methodology that allows obtaining accurate results from *in situ* powder diffraction and microtomography. It has been shown above that the RQPA results arising from the *in situ* MoKα_1 LXRPD study, for a CEM I 42.5 R, are relatively accurate, as the comparison with *ex situ* LXRPD data and thermal data were very satisfactory. Hence, sample preparation and *in situ* LXRPD data acquisition and data analysis were validated. The reason for the choice of this PC, i.e. 42.5 R, in contrast to the more commonly used, 52.5 R (or N), was its slightly coarse particle size distribution. As reported in the experimental section, $D_{v,50}$ for the cement employed, in this proof-of-principle work, was ~17 µm. 52.5 PCs have smaller $D_{v,50}$ values ranging from ~10 to 14 µm. This means a higher fraction of particles smaller than ~2.5 µm than cannot be directly detected by µCT. The *in situ* study of a CEM I 52.5 R, with different w/c mass ratios, is currently underway and the results will be reported elsewhere. Next, we focus on the comparison of the *in situ* RQPA results with the *in situ* µCT results for the employed PC 42.5.

In order to carry out this comparison, firstly the contents given in Table 5, in wt%, determined/calculated from LXRPD are transformed to vol% taking into account the known densities for all the components. Thus, Table 9 displays the contents both in cm^3 refereed to 100 g of cement paste and in vol%. It is noted that 100 cm^3 of a paste is not a constant basis in cement hydration because of the difference in volumes between reactants and productski. Once the paste sets, this decrease in volume is shared between the bulk volume shrinkage and internal gas (air/water) porosity development. It is noted that C-S-H gel would be around 35 vol% of the paste when expressed as $(CaO)_{1.8}SiO_2(H_2O)_{4.0}$, i.e. containing the gel pore water but not containing the free-water/capillary-water. Because of the fine intermixing of C-S-H and capillary water, if these two components are considered together, this would be around 60 vol% of the paste. Moreover, this means that any diffraction study of cement pastes is blind to more than 60 % of the volume of the probed sample. However, features like portlandite content increase and alite amount decrease can be accurately determined by LXRPD if the employed experimental approach is robust enough.

15

For the comparison between the LXRPD and μCT results, the anhydrous cement components have been gathered, i.e. C_3S, C_2S, C_3A, C_4AF and $C\underline{C}$. From the LAC point of view, it is not currently clear if $C\underline{C}$ is below or above the crossing point at 20500 grey value. This is the subject of an ongoing investigation which has also the goal to expand this approach to Portland-Limestone cements. In any case, the amount of calcite is minor in the investigated PC, and therefore this choice should not severely bias the results. For the ML results, the hd-HP and ld-HP are summed for easier comparison. The results are shown in Table 10. Here, the implications of the small differences in the evolving overall volume up to 7 days are not considered, as they are likely within the errors of the segmentations.

Table 9

In situ RQPA results for the PC 42.5 pastes, w/c=0.50, expressed in cm^3 (referred to 100 g of cement paste). The mass densities used for the transformation are also reported. The corresponding values in vol% are given in italics, but 100 cm^3 of paste is not a constant basis in a hydrating cement.

phases	ρ / gcm^{-3}	t_0/ cm^3	t_0/vol%	1d/ cm^3	1d/vol%	3d/ cm^3	3d/vol%	7d/ cm^3	7d/vol%	77d/ cm^3	77d/vol%
C_3S	3.15	12.18	*22.4*	4.79	*9.1*	2.34	*4.5*	1.95	*3.8*	1.29	*2.5*
C_2S	3.30	2.59	*4.8*	2.47	*4.7*	2.55	*4.9*	2.45	*4.7*	2.22	*4.3*
C_3A	3.05	1.46	*2.7*	0.70	*1.3*	0.32	*0.6*	0.16	*0.3*	0.09	*0.2*
C_4AF	3.73	1.82	*3.4*	1.63	*3.1*	1.21	*2.3*	1.17	*2.3*	0.97	*1.9*
$C\underline{C}$	2.71	1.29	*2.4*	1.73	*3.3*	1.86	*3.6*	1.75	*3.4*	1.83	*3.5*
minors	-	1.67	*3.0*	0.20	*0.4*	0.11	*0.2*	0.14	*0.3*	0.14	*0.3*
H_2O	1.00	33.33	*61.3*	19.13	*36.4*	14.99	*28.8*	13.87	*26.7*	12.48	*24.1*
AFt	1.78		-	5.03	*9.6*	5.74	*11.0*	5.99	*11.5*	6.18	*11.9*
CH	2.23		-	4.02	*7.6*	5.24	*10.1*	5.62	*10.8*	5.96	*11.5*
C-S-H	2.11		-	12.37	*23.5*	16.04	*30.8*	17.00	*32.7*	18.07	*34.9*
Fe-Si-Hg	2.52		-	0.49	*0.9*	1.61	*3.1*	1.70	*3.3*	2.22	*4.3*
Hc	1.90		-	-	-	0.08	*0.2*	0.13	*0.2*	0.07	*0.1*
Mc	2.22		-	-	-	-	-	-	-	0.25	*0.5*
total:		54.36	*100.0*	52.55	*100.0*	52.08	*100.0*	51.94	*100.0*	51.78	*100.0*

Table 10 allows to initially discuss the ML and GT results. At 1 day and later, the results are quite similar. At 12 h this is not the case as the UCP contents are 28.7 and 22.8 vol% for ML and GT, respectively. There are no available results from LXRPD at this age, but the overall PC degree of hydration can be calculated considering the UCP content at the time of mixing, i.e. 35.6 vol%. The PC DoHs are 36 and 19% for GT and ML results, respectively. The DoH at 12 h from GT is too high and this result seems to be inaccurate.

The comparison between the UCP contents from *in situ* LXRPD and *in situ* μCT has to be exercised with care as the data are not taken simultaneously but sequentially. This means that there is always a delay between both sets of measurements. With our employed experimental conditions, *in situ* LXRPD were taken 3 hours later than the corresponding μCT measurements. This is important at 1 day, when the reactions are fast, and likely negligible at 7 days or later when the hydration kinetics are very slow. With this caveat, the agreement between UCP contents from LXRPD and μCT are within 2.3 wt% at 1 day and within 1.5% at later hydration ages. This disagreement/error is considered acceptable and means that the UCP results from μCT data analysed both by GT and ML are relatively accurate. Global thresholding is easier to do from the methodological point of view. However, the final aim of this investigation is to be able to use μCT for helping to determine the reaction degree of SCMs. In this case, the LAC of most SCMs is located within the HP peaks and global thresholding is not useful. Conversely, ML profits from the LAC/grey-values and the local features such as particle shapes and homogeneity within the reconstructed volume. Therefore, for the long-term development of this approach to obtain relevant scientific results, ML segmentation is judged to be much superior.

Table 10

Comparison of RQPA and µCT results in vol%. The outputs for the µCT study have been renormalized to leave out the (air) porosities, i.e. the results are shown respect to the HP and UCP contents.

hydration age	components	LXRPD	GT	ML*
t_0	HP	64.4	-	-
	UCP	35.6	-	-
12h	HP	-	77.2	71.3
	UCP	-	22.8	28.7
1d	HP	78.5	79.9	76.2
	UCP	21.5	20.1	23.8
3d	HP	84.1	84.0	83.2
	UCP	15.9	16.0	16.8
7d	HP	85.5	84.8	84.2
	UCP	14.5	15.2	15.8
79d	HP	87.6	86.6	87.1
	UCP	12.4	13.4	12.9

*ld-HP and hd-HP derived from ML have been summed as a single hydrate product (HP) for comparison to global-thresholding and LXRPD results.

5. Conclusions.

This investigation reports an accurate experimental protocol for *in situ* cement hydration studies avoiding any alteration after mixing due to sample conditioning. The pastes are just injected within thick glass capillaries/tubes, nominal diameter of 2.0 mm, and both ends are sealed. The thick capillaries are vital to have very good powder averaging and to avoid self-desiccation. The sealing avoids any water loss and portlandite carbonation. The paste rotation within a capillary minimises portlandite prefer orientation. The pastes are sequentially analysed by X-ray microtomography and MoKα_1 X-ray powder diffraction.

Results for a w/c=0.50 paste, made out of a commercial PC 42.5, are reported. To determine the accuracy of the proposed *in situ* methodology, the same sample was cured *ex situ* and also quantitatively studied by thermal analysis and powder diffraction. Portlandite contents were 13.8, 13.1 and 12.5 wt% by thermal analysis, *ex situ* powder diffraction and *in situ* powder diffraction, respectively. Moreover, a mass balance calculation from the reacted fractions of C_3S and C_4AF yielded 13.1 wt% of CH. AFt keeps growing with time up to 77 days without any sign of partial transformation to AFm, despite the lack of sulfates at later hydration ages. The second stream of this study was to collect microtomographic data in exactly the same region of the hydrating paste. This minimises the variability in the obtained results and shows a crossing, invariant, point in the grey-value histogram evolution with time. Segmentations have been carried out by global thresholding and the random forest method. The comparison of the segmented results for the unhydrated cement particles and the Rietveld quantitative phase analysis outputs indicate an agreement within 2 %.

In a nutshell, here it is proposed an innovative and accurate methodology, based on *in situ* X-ray powder diffraction and microtomography, with potential to determine binder reaction degrees with smaller errors and the possibility for automatize data analysis. This approach is developed to analyse more challenging binders, PC-SCMs, which will be the subject of forthcoming publications.

References

[1]   H.F.W. Taylor, Cement chemistry. 2nd ed., Acad. Press. 20 (1997) 335. https://doi.org/10.1016/S0958-9465(98)00023-7.

[2]   P.C. Hewlett, M. Liska, Lea's Chemistry of Cement and Concrete, 5th ed., Elsevier, 2017.

[3]   K.L. Scrivener, R. Snellings, B. Lothenbach, A Practical Guide to Microstructural Analysis of Cementitious Materials, CRC Press, Boca Raton, FL, 2016.

[4]   A.G. De la Torre, A. Cabeza, A. Calvente, S. Bruque, M.A.G. Aranda, Full phase analysis of portland clinker by penetrating synchrotron powder diffraction, Anal. Chem. 73 (2001) 151–156. https://doi.org/10.1021/ac0006674.

[5]   M.A.G. Aranda, A.G. De la Torre, L. Leon-Reina, Rietveld Quantitative Phase Analysis of OPC Clinkers, Cements and Hydration Products, Rev. Mineral. Geochemistry. 74 (2012) 169–209. https://doi.org/10.2138/rmg.2012.74.5.

[6]   D. Jansen, C. Stabler, F. Goetz-Neunhoeffer, S. Dittrich, J. Neubauer, Does Ordinary Portland Cement contain amorphous phase? A quantitative study using an external standard method, Powder Diffr. 26 (2011) 31–38. https://doi.org/10.1154/1.3549186.

[7]   L. León-Reina, A.G. De la Torre, J.M. Porras-Vázquez, M. Cruz, L.M. Ordonez, X. Alcobé, F. Gispert-Guirado, A. Larrãaga-Varga, M. Paul, T. Fuellmann, R. Schmidt, M.A.G. Aranda, Round robin on Rietveld quantitative phase analysis of Portland cements, J. Appl. Crystallogr. 42 (2009) 906–916. https://doi.org/10.1107/S0021889809028374.

[8]   G. Le Saoût, V. Kocaba, K. Scrivener, Application of the Rietveld method to the analysis of anhydrous cement, Cem. Concr. Res. 41 (2011) 133–148. https://doi.org/10.1016/j.cemconres.2010.10.003.

[9]   D. Jansen, F. Goetz-Neunhoeffer, C. Stabler, J. Neubauer, A remastered external standard method applied to the quantification of early OPC hydration, Cem. Concr. Res. 41 (2011) 602–608. https://doi.org/10.1016/j.cemconres.2011.03.004.

[10]   A.G. De la Torre, S. Bruque, M.A.G. Aranda, Rietveld quantitative amorphous content analysis, J. Appl. Crystallogr. 34 (2001) 196–202. https://doi.org/10.1107/S0021889801002485.

[11]   P.J. Withers, C. Bouman, S. Carmignato, V. Cnudde, D. Grimaldi, C.K. Hagen, E. Maire, M. Manley, A. Du Plessis, S.R. Stock, X-ray computed tomography, Nat. Rev. Methods Prim. 2021 11. 1 (2021) 1–21. https://doi.org/10.1038/s43586-021-00015-4.

[12]   Í.B. da Silva, X-ray Computed Microtomography technique applied for cementitious materials: A review, Micron. 107 (2018) 1–8. https://doi.org/10.1016/j.micron.2018.01.006.

[13]   A. du Plessis, W.P. Boshoff, A review of X-ray computed tomography of concrete and asphalt

621   construction materials, Constr. Build. Mater. 199 (2019) 637–651.
622   https://doi.org/10.1016/j.conbuildmat.2018.12.049.

623 [14] S. Brisard, M. Serdar, P.J.M. Monteiro, Multiscale X-ray tomography of cementitious materials: A
624   review, Cem. Concr. Res. 128 (2020) 105824. https://doi.org/10.1016/j.cemconres.2019.105824.

625 [15] W. Kong, Y. Wei, S. Wang, J. Chen, Y. Wang, Research progress on cement-based materials by X-
626   ray computed tomography, Int. J. Pavement Res. Technol. 13 (2020) 366–375.
627   https://doi.org/10.1007/s42947-020-0119-8.

628 [16] T. Sugiyama, M.A.B. Promentilla, Advancing concrete durability research through X-ray computed
629   tomography, J. Adv. Concr. Technol. 19 (2021) 730–755. https://doi.org/10.3151/jact.19.730.

630 [17] S.Y. Chung, J.S. Kim, D. Stephan, T.S. Han, Overview of the use of micro-computed tomography
631   (micro-CT) to investigate the relation between the material characteristics and properties of cement-
632   based materials, Constr. Build. Mater. 229 (2019) 116843.
633   https://doi.org/10.1016/j.conbuildmat.2019.116843.

634 [18] I.R. Salcedo, A. Cuesta, S. Shirani, L. León-Reina, M.A.G. Aranda, Accuracy in Cement Hydration
635   Investigations: Combined X-ray Microtomography and Powder Diffraction Analyses, Mater. 2021,
636   Vol. 14, Page 6953. 14 (2021) 6953. https://doi.org/10.3390/MA14226953.

637 [19] S. Shirani, A. Cuesta, A. Morales-Cantero, I. Santacruz, A. Diaz, P. Trtik, M. Holler, A. Rack, B.
638   Lukic, E. Brun, I.R. Salcedo, M.A.G. Aranda, 4D nanoimaging of early age cement hydration, Nat.
639   Commun. 14 (2023) 2652. https://doi.org/10.1038/s41467-023-38380-1.

640 [20] A. Cuesta, S. Shirani, A.G. De la Torre, I. Santacruz, A. Morales-Cantero, I. Koufany, C. Redondo-
641   Soto, I.R. Salcedo, L. Leon-Reina, M.A.G. Aranda, Combined use of laboratory X-ray diffraction and
642   microtomography in early age cement hydration, in: Proc. 16th Int. Congr. Chem. Cem., Bangkok,
643   2023: p. accepted (to be published in September).

644 [21] M. García-Maté, A.G. De la Torre, L. León-Reina, E.R. Losilla, M.A.G. Aranda, I. Santacruz, Effect
645   of calcium sulfate source on the hydration of calcium sulfoaluminate eco-cement, Cem. Concr.
646   Compos. 55 (2015) 53–61. https://doi.org/10.1016/j.cemconcomp.2014.08.003.

647 [22] J.D. Zea-Garcia, I. Santacruz, M.A.G. Aranda, A.G. De la Torre, Alite-belite-ye'elimite cements:
648   Effect of dopants on the clinker phase composition and properties, Cem. Concr. Res. 115 (2019) 192–
649   202. https://doi.org/https://doi.org/10.1016/j.cemconres.2018.10.019.

650 [23] A.C. Larson, R.B. Von Dreele, General structure analysis system (GSAS), Los Alamos Natl. Lab.
651   Rep. LAUR. 748 (2004) 86–748.

652 [24] P. Thompson, D.E. Cox, J.B. Hastings, Rietveld Refinement of Debye-Scherrer Synchrotron X-ray
653   Data from A1203, J. Appl. Crystallogr. 20 (1987) 79–83.
654   https://doi.org/10.1107/S0021889887087090.

655 [25] L.W. Finger, D.E. Cox, A.P. Jephcoat, Correction for powder diffraction peak asymmetry due to axial
656   divergence, J. Appl. Crystallogr. 27 (1994) 892–900. https://doi.org/10.1107/S0021889894004218.

657 [26] A.G. De la Torre, I. Santacruz, A. Cuesta, L. León-Reina, M.A.G. Aranda, Diffraction and
658   crystallography applied to anhydrous cements, in: H. Pöllmann (Ed.), Cem. Mater., De Gruyter, 2017:
659   pp. 3–29.

660 [27] M.A.G. Aranda, A. Cuesta, A.G. De la Torre, I. Santacruz, L. León-Reina, Diffraction and
661   crystallography applied to hydrating cements, in: H. Pöllmann (Ed.), Cem. Mater. Compos. Prop.
662   Appl., De Gruyter, Berlin, Boston, Germany, 2017: pp. 31–60.
663   https://doi.org/10.1515/9783110473728-003.

664 [28] A.G. De la Torre, S. Bruque, J. Campo, M.A.G. Aranda, The superstructure of C3S from synchrotron
665   and neutron powder diffraction and its role in quantitative phase analyses, Cem. Concr. Res. 32
666   (2002) 1347–1356.

667   [29]   W.G. Mumme, R.J. Hill, G. Bushnell-Wye, E.R. Segnit, Rietveld crystal structure refinements,
668   crystal chemistry and calculated powder diffraction data for the polymorphs of dicalcium silicate and
669   related phases, Neues Jahrb. Fuer Mineral. 169 (1995) 35–68.

670   [30]   Y. Takéuchi, F. Nishi, Crystal-chemical characterization of the 3CaO·Al2O3—Na2O solid-solution
671   series, Zeitschrift Für Krist. - Cryst. Mater. 152 (1980) 259–308.
672   https://doi.org/10.1524/zkri.1980.152.14.259.

673   [31]   A.A. Colville, S. Geller, The Crystal Structure of Brownmillerite, Ca2FeAlO5, Acta Cryst. 27 (1971)
674   5. https://doi.org/10.1107/S056774087100579X.

675   [32]   C. Bezou, A. Nonat, J.-C. Mutin, A.N. Christensen, M.S. Lehmann, Investigation of the Crystal
676   Structure of γ-CaSO4, CaSO4 0.5H2O, and CaSO4·0.6H2O by Powder Diffraction Methods, J. Solid
677   State Chem. 117 (1995) 165–176. https://doi.org/10.1006/JSSC.1995.1260.

678   [33]   A.G. De la Torre, M.-G. López-Olmo, C. Álvarez-Rua, S. García-Granda, M.A.G. Aranda, Structure
679   and microstructure of gypsum and its relevance to Rietveld quantitative phase analyses, Powder Diffr.
680   19 (2004) 240–246.

681   [34]   E.N. Maslen, V.A. Streltsov, N.R. Streltsova, N. Ishizawa, Electron density and optical anisotropy in
682   rhombohedral carbonates. III. Synchrotron X-ray studies of CaCO3, MgCO3 and MnCO3, Acta
683   Crystallogr. Sect. B. 51 (1995) 929–939. https://doi.org/10.1107/S0108768195006434.

684   [35]   G. Will, M. Bellotto, W. Parrish, M. Hart, Crystal structures of quartz and magnesium germanate by
685   profile analysis of synchrotron-radiation high-resolution powder data, J. Appl. Crystallogr. 21 (1988)
686   182–191. https://doi.org/10.1107/S0021889887011567/FULL.

687   [36]   F. Goetz-Neunhoeffer, J. Neubauer, Refined ettringite (Ca6Al2(SO4)3(OH)12·26HO) structure for
688   quantitative X-ray diffraction analysis, Powder Diffr. 21 (2006) 4–11.
689   https://doi.org/10.1154/1.2146207.

690   [37]   O. Chaix-Pluchery, J. Pannetier, J. Bouillot, J.C. Niepce, Structural prereactional transformations in
691   Ca(OH)2, J. Solid State Chem. 67 (1987) 225–234. https://doi.org/10.1016/0022-4596(87)90358-6.

692   [38]   T. Runčevski, R.E. Dinnebier, O. V. Magdysyuk, H. Pöllmann, Crystal structures of calcium
693   hemicarboaluminate and carbonated calcium hemicarboaluminate from synchrotron powder
694   diffraction data, Acta Crystallogr. Sect. B Struct. Sci. (2012).
695   https://doi.org/10.1107/S010876811203042X.

696   [39]   E. Qoku, K. Xu, J. Li, P.J.M. Monteiro, K.E. Kurtis, Advances in Imaging, Scattering, Spectroscopy,
697   and Machine Learning-Aided Approaches for Multiscale Characterization of Cementitious Systems,
698   Cem. Concr. Res. 174 (2023) 107335. https://doi.org/10.1016/j.cemconres.2023.107335.

699   [40]   A. Cuesta, J.D. Zea-Garcia, D. Londono-Zuluaga, A.G. De la Torre, I. Santacruz, O. Vallcorba, M.
700   Dapiaggi, S.G. Sanfélix, M.A.G. Aranda, Multiscale understanding of tricalcium silicate hydration
701   reactions, Sci. Rep. 8 (2018) 8544. https://doi.org/10.1038/s41598-018-26943-y.

702   [41]   F. Avet, X. Li, K.L. Scrivener, Determination of the amount of reacted metakaolin in calcined clay
703   blends, Cem. Concr. Res. 106 (2018) 40–48. https://doi.org/10.1016/J.CEMCONRES.2018.01.009.

704   [42]   F. Zunino, Y. Dhandapani, M. Ben Haha, J. Skibsted, S. Joseph, S. Krishnan, A. Parashar, M.C.G.
705   Juenger, T. Hanein, S.A. Bernal, K.L. Scrivener, F. Avet, Hydration and mixture design of calcined
706   clay blended cements: review by the RILEM TC 282-CCL, Mater. Struct. Constr. 55 (2022) 234.
707   https://doi.org/10.1617/s11527-022-02060-1.

708   [43]   S. Shirani, A. Cuesta, A. Morales-Cantero, A.G. De la Torre, M.P. Olbinado, M.A.G. Aranda,
709   Influence of curing temperature on belite cement hydration: A comparative study with Portland
710   cement, Cem. Concr. Res. 147 (2021) 106499. https://doi.org/10.1016/j.cemconres.2021.106499.

711   [44]   S. Shirani, C. Redondo-soto, I.M.R. Bernal, A. Cuesta, I. Santacruz, A.G. De La Torre, I.R. Salcedo,
712   M.P. Olbinado, M.A.G. Aranda, X-ray Microtomographic Studies of LC3 and Related Binders, in:
713   Proc. Int. Conf. Calcined Clays Sustain. Concr. 2022, 2022: p. accepted.

714   [45]   J. Zhang, G.W. Scherer, Comparison of methods for arresting hydration of cement, Cem. Concr. Res.
715   41 (2011) 1024–1036. https://doi.org/10.1016/j.cemconres.2011.06.003.

716   [46]   I. Galan, H. Beltagui, M. García-Maté, F.P. Glasser, M.S. Imbabi, Impact of drying on pore structures
717   in ettringite-rich cements, Cem. Concr. Res. 84 (2016) 85–94.
718   https://doi.org/10.1016/j.cemconres.2016.03.003.

719   [47]   R. Snellings, J. Chwast, Ö. Cizer, N. De Belie, Y. Dhandapani, P. Durdzinski, J. Elsen, J. Haufe, D.
720   Hooton, C. Patapy, M. Santhanam, K. Scrivener, D. Snoeck, L. Steger, S. Tongbo, A. Vollpracht, F.
721   Winnefeld, B. Lothenbach, Report of TC 238-SCM: hydration stoppage methods for phase
722   assemblage studies of blended cements—results of a round robin test, Mater. Struct. Constr. 51
723   (2018). https://doi.org/10.1617/s11527-018-1237-5.

724   [48]   A. Mezhov, D. Kulisch, A. Goncharov, S. Zhutovsky, A Comparative Study of Factors Influencing
725   Hydration Stoppage of Hardened Cement Paste, Sustain. 15 (2023) 1080.
726   https://doi.org/10.3390/su15021080.

727   [49]   C. Donnelly, S. Finizio, S. Gliga, M. Holler, A. Hrabec, M. Odstrčil, S. Mayr, V. Scagnoli, L.J.
728   Heyderman, M. Guizar-Sicairos, J. Raabe, Time-resolved imaging of three-dimensional nanoscale
729   magnetization dynamics, Nat. Nanotechnol. 15 (2020) 356–360. https://doi.org/10.1038/s41565-020-
730   0649-x.

731   [50]   X. Li, Q. Hu, B. Robertson, M.T. Ley, V.J. De Andrade, G. Sokhansefat, Direct observation of C3S
732   particle dissolution using fast nano X-ray computed tomography, Cem. Concr. Res. 166 (2023)
733   107097. https://doi.org/10.1016/j.cemconres.2023.107097.

734   [51]   M.A.G. Aranda, Recent studies of cements and concretes by synchrotron radiation crystallographic
735   and cognate methods, Crystallogr. Rev. 22 (2016) 150–196.
736   https://doi.org/10.1080/0889311X.2015.1070260.

737   [52]   O. Linderoth, L. Wadsö, D. Jansen, Long-term cement hydration studies with isothermal calorimetry,
738   Cem. Concr. Res. 141 (2021) 106344. https://doi.org/10.1016/j.cemconres.2020.106344.

739